1 **A molecular brain atlas reveals cellular shifts during the repair phase**

2 **of stroke**

3

4 Abstract

5 Rebecca Z Weber[1,2], Beatriz Achón Buil[1,2], Nora H Rentsch[1,2], Allison Bosworth[3,4], Mingzi

6 Zhang[3,4], Kassandra Kisler[3,4], Christian Tackenberg[1,2], Berislav V Zlokovic[3,4], Ruslan Rust[1,2,3,4]

7

8 [1] Institute for Regenerative Medicine, University of Zurich, Schlieren, Switzerland,

9 [2] Neuroscience Center Zurich, ETH Zurich and University of Zurich, Zurich, Switzerland

10 [3] Department of Physiology and Neuroscience, University of Southern California, Los Angeles,

11 USA

12 [4] Zilkha Neurogenetic Institute, Keck School of Medicine, University of Southern California,

13 Los Angeles, USA

14

15

16 Correspondence

17 Ruslan Rust

18 rrust@usc.edu

19 **Abstract**

20 Ischemic stroke triggers a cascade of pathological events that affect multiple cell types and
21 often lead to incomplete functional recovery. Despite advances in single-cell technologies, the
22 molecular and cellular responses that contribute to long-term post-stroke impairment remain
23 poorly understood. To gain better insight into the underlying mechanisms, we generated a
24 single-cell transcriptomic atlas from distinct brain regions using a mouse model of permanent
25 focal ischemia at one month post-injury. Our findings reveal cell- and region-specific changes
26 within the stroke-injured and peri-infarct brain tissue. For instance, GABAergic and
27 glutamatergic neurons exhibited upregulated genes in signaling pathways involved in axon
28 guidance and synaptic plasticity, and downregulated pathways associated with aerobic
29 metabolism. Using cell-cell communication analysis, we identified increased strength in
30 predicted interactions within stroke tissue among both neural and non-neural cells via
31 signaling pathways such as those involving collagen, protein tyrosine phosphatase receptor,
32 neuronal growth regulator, laminin, and several cell adhesion molecules. Furthermore, we
33 found a strong correlation between mouse transcriptome responses after stroke and those
34 observed in human nonfatal brain stroke lesions. Common molecular features were linked to
35 inflammatory responses, extracellular matrix organization, and angiogenesis. Our findings
36 provide a detailed resource for advancing our molecular understanding of stroke pathology
37 and for discovering therapeutic targets in the repair phase of stroke recovery.

38

Introduction

39

40   Stroke remains a leading cause of disability and death, affecting one in four adults in
41   their lifetime[1,2]. Over half of stroke patients are left with permanent disabilities including partial
42   paralysis and cognitive deficits due to the brain's limited ability to regenerate damaged neural
43   circuits. Post-stroke damage develops from a complex interplay of pathological processes that
44   involve all major cellular components of the brain including neurons, glia cells, resident and
45   infiltrating immune cells, blood vessels, and peri-vascular mural cells.[3] Each cell type
46   undergoes significant changes in response to stroke and the contributions of individual cell
47   types to recovery remain not fully understood. Some cellular responses were associated with
48   enhances recovery, while others may be detrimental[4–7]. These phenotypic alterations are often
49   regulated at the transcriptional level.

50   Several single cell/nucleus RNA sequencing studies characterized the cellular
51   heterogeneity in the healthy human and mouse brain[8–14]. Recent cellular atlases were
52   generated in response to several neurodegenerative diseases[15–17] and acute neurological
53   injuries including spinal cord injury and stroke, supporting the functional plasticity of individual
54   brain cells[18–21]. Some molecular stroke atlases focused characterization of single cell types
55   e.g., immune cells, pericytes or vascular cells[18,19,22], some used acute time points[22–24] and
56   none looked at a permanent focal ischemia mouse model.

57   Therefore, we performed snRNAseq on mouse brains one-month post-stroke using a
58   mouse model that simulates permanent stroke conditions to (a) generate a molecular atlas of
59   cell types from stroke-injured and peri-infarct regions, (b) infer molecular communication
60   networks among individual cells and (c) compare these transcriptomic changes to those
61   observed in human chronic, non-fatal brain stroke lesions. These findings enhance our
62   mechanistic understanding of stroke repair and may improve therapeutic targeting during the
63   transition phase of subacute to chronic stroke.

Results

Cellular and molecular profiles of adult intact, peri-infarct and stroke-injured brain

To molecularly profile the stroke-injured brain, we induced large cortical strokes in the sensorimotor cortex of C57BL/6J mice (**Fig 1A**). All mice showed a severe ≈70% reduction in cerebral blood flow in the stroke core, and ≈45% reduction in the ischemic border zone (ibz) compared to the intact hemisphere at 2 h after stroke induction (**Fig 1B, C**).

Four weeks after stroke, we performed a microbiopsy of a) intact, b) ibz, and c) stroke core tissue. All samples were processed for single nucleus RNA sequencing (snRNAseq) using the 10X Genomics Chromium platform, generating transcriptomes from approximately 35,000 nuclei (**Fig 1D**).

We performed clustering and annotation of nine major cell populations of the mouse brain guided by the known marker expression patterns from molecular atlases[11,17,25] : Glutamatergic neurons (Glut: e.g., Slc17a7, Satb2), GABAergic neurons (GABA: e.g. Gad1, Gad2), astrocytes (Asc: Slc1a2, Slc1a3), fibroblasts (FB: Col1a, Fn1), oligodendrocytes (Olig: Mbp, Plp1), immune cells (Imm: Inpp5d, Csf1r), vascular cells (Vasc: Flt1, Cldn5), stem and progenitor cells (SPC: Sox10, Vcan), and mural cells (Per: Pdgfrb, Cspg4) (**Fig. 1E**). These cell types and marker expression of cell types matched previous single-cell/snRNAseq data from adult non-injured mouse cortices[12,26,27].

We used these cell-type categories from the intact adult mouse brain to characterize changes specific to ibz and stroke-injured brain tissue (**Fig 1F-H**). All cell types were determined with a >99% confidence in all datasets. We observe an increase in the proportion of non-neural cells in the ibz (+12%) and in the stroke-injured tissue (+66%, **Fig. 1I**). Notably, the ratio of both glutamatergic and GABAergic cells to the total cell population was reduced in the stroke-injured tissue (Glut: intact: 82%, ibz: 58%, stroke: 10%: GABA: intact: 12%, ibz: 14%, stroke: 8%), whereas the relative number of certain non-neural cell types increased especially e.g., fibroblasts (intact: 1%, ibz: 1%, stroke: 22%), astrocytes (intact: 4%, ibz: 12%, stroke: 14%), oligodendrocytes (intact: 2%, ibz: 7%, stroke: 9%), vascular cells (intact:1%, ibz: 3%, stroke: 6%) and immune cells (intact:1%, ibz: 2%, stroke: 7%, **Fig. 1J**).

In addition, we aimed to confirm the abundance of major cell populations in immunohistochemical stainings of intact and stroke brain tissue. We selected markers specific to mature neurons (NeuN^{+}), astrocytes (GFAP^{+}), macrophages (CD68^{+}), microglia (Iba-1^{+}), endothelial cells (CD31^{+}) and pericytes (CD13^{+}) and stained stroked and intact coronal brain sections 28 days after injury (**Fig. 1K**). We found that relative NeuN^{+} expression was significantly reduced in stroke-injured and ibz tissue, whereas GFAP^{+}-expression increased in the ibz compared to the intact side. CD68^{+}, highly expressed in macrophages[28], and IBA1^{+},

100 expressed in microglia/monocytes[23], was found to be elevated in the stroke core and the ibz

101 after injury, compared to marker expression in intact tissue. Interestingly, we also found

102 increase in CD13^{+} signals in the stroke core that were not associated with CD31^{+} vasculature,

103 potentially indicating recently described CD13^{+} infiltrating monocytes which have been

104 described to aggravate acute stroke injure but promote chronic post-stroke recovery.[29]

105 Although the relative number of vascular cells, compared to other cell types, increased in the

106 stroke snRNAseq dataset, the overall coverage of CD31^{+} vasculature in stroke tissue is lower

107 in the injured hemisphere compared to the intact hemisphere, consistent with previous stroke

108 studies[30–33].

109 Analysis of neural subtypes using snRNAseq revealed a decrease in most

110 glutamatergic and GABAergic subclusters in stroke-injured tissue (**Fig. 1M**). For instance, the

111 ratio of GABAergic parvalbumin (PV)-expressing, vasoactive intestinal polypeptide (Vip)-

112 expressing, and somatostatin (Sst)-expressing neurons, as well as glutamatergic layer 2/3

113 and layer 6 intratelencephalic (IT) neurons was reduced by >80% relative to the intact tissue.

114 These findings align with previous functional studies showing that the loss of specific

115 interneurons, such as PV and SST-expressing neurons, can worsen stroke outcomes and

116 rescuing these populations may serve as a therapeutic target[34–37].

117 Additionally, within the stroke core tissue, we identified a distinct cluster of cells, absent

118 in the intact tissue, which we have termed 'injury-associated cells' (IC) (**Fig. 1J, N**). IC cells

119 are positive for astrocytic markers such as Apoe and Slc1a2 but also express genes related

120 to ECM modeling such as Col1a2 and Col3a1. ICs transcriptionally segregated from other

121 clusters by expression of genes involved in formation of scar tissue e.g., Dcn, Lum, Col3a1,

122 and Col1a1, but also promotion of remodeling and tissue repair e.g., Mmp14, Vim, Igfbp5, and

123 Sparc. Correlation analysis between all cell types revealed that the IC cell cluster shows most

124 gene expression similarities (r = 0.85) to astrocytes and fibroblasts (**Fig. 1O**). Next, we

125 selected one of the top IC markers and stained intact and stroked coronal brain sections (**Fig.**

126 **1P, Q**). We found that insulin like growth factor binding protein 5 (Igfbp5) was strongly

127 expressed within the infarction core, but barely in the intact hemisphere (**Fig. 1P, Q**).

128 IC may represent a reactive or reparative cell type, such as reactive glia or fibroblasts,

129 which have been shown to become proliferate and activated in response to CNS injury[38–41].

130 Importantly, ICs did also not show expression of canonical markers associated with fibrotic

131 pericytes[4].

132

Fig 1: Cellular profiling of the stroke-injured mouse brain. (A) Scheme of experimental workflow **(B)** Laser Doppler imaging (LDI) illustrating relative perfusion in the mouse brain **(C)** Bar plot showing quantification of relative blood perfusion in the stroke core and the ischemic border zone (ibz) compared to the left hemisphere acutely after stroke **(D)** Illustration of brain regions for biopsy to perform snRNAseq **(E)** Dot plot representation of canonical cell type markers across different cell populations from the intact contralesional hemisphere, labeled by cell type: glutamatergic neurons (Glut), GABAergic neurons (GABA), astrocytes (Asc), fibroblasts (FB), oligodendrocytes (Olig), immune cells (Imm), vascular cells (Vasc), stem/progenitor cells (SPC), and mural cells (Per) **(F-H)** UMAP visualization of cell clusters from intact, ibz and stroke tissue. **(I)** Bar plot showing distribution of cell type by neural and non-neural cells and individual cell types **(J)** across the reference, intact, ibz and stroke samples. **(K)** Representative histological overview of brain sections stained with (from left to right) Gat/vGlut, IBA1/GFAP, CD68/IBA1, CD31/CD13, co-stained with DAPI. **(L)** Quantification of NeuN+, GFAP+, IBA1+, CD68+, CD31+ and CD13+ expression relative to intact tissue (dotted line). **(M)** Bar graph showing relative amount of major GABA and glutamatergic neuronal subtypes. **(N)** Dot plot showing expression of canonical cell type marker of injury-associated cells (IC), FB, and Asc. **(O)** Heatmap showing correlation of gene expression profiles between each cell type from stroke tissue. **(P)** Representative histological overview of brain sections stained with IGFBP5 (left) and quantification of IGFBP5 expression relative to intact tissue (right). **(Q)** Feature plot showing the expression patterns of Apoe, Adam12, Cola1a2, and Vim in cells from stroke tissue. The data was generated with a cohort of n = 9 mice.

Transcriptomic shift and pathway enrichment in brain cells following stroke

Next, we examined how long-term cerebral ischemia affects gene expression and pathway enrichment in individual brain cells (**Fig 2A**). We found that most cell types exhibited differentially expressed genes (DEG) after stroke. As expected, most DEG were observed between nuclei from stroke-injured brains compared to intact tissue. Most DEGs were observed in FB, Glut and GABA nuclei (**Fig 2A**). Interestingly, most DEGs overlapped between stroke/intact and ibz/intact tissue for neural (Glut and GABA) nuclei (**Fig 2B**), whereas non-neural cells exhibited a more distinct, regional-specific DEG signature (**Fig 2C**).

Gene set-enrichment analysis (GSEA) revealed that upregulated pathways in GABA and Glut neural cells predominantly involved pro-regenerative responses including synaptic plasticity, neurotransmitter transport, synapse organization, and axon guidance (all $p < 0.001$), while downregulated pathways in all neural cells included aerobic respiration and oxidative phosphorylation (**Fig. 2 D, E**; all $p < 0.001$). This shift in cellular metabolism from energy-efficient aerobic respiration to alternative metabolic processes may potentially reflect an adaptive response to the altered microenvironment post-stroke[42].

Immune cells mainly showed an upregulation in inflammation-associated pathways such as leukocyte activation and positive regulation of immune response (all $p < 0.001$). Notably, immune cells were the only cell types that did not exhibit altered aerobic metabolism (**Fig 2F**).

Astrocytes and fibroblasts revealed enrichment in pathways linked to remodeling such as extracellular matrix (ECM) organization and cell adhesion and migration processes (all $p < 0.001$) (**Fig 2 G, H**). Additionally, ECs showed enrichment in angiogenesis and remodeling pathways, alongside a downregulated in aerobic metabolism (**Fig 2I**; all $p < 0.001$).

Together, these data suggest major transcriptional changes of all major brain cells at 28 days after stroke involving pro-regenerative and remodeling pathways, while also indicating a persistently inflammatory and hypoxic environment.
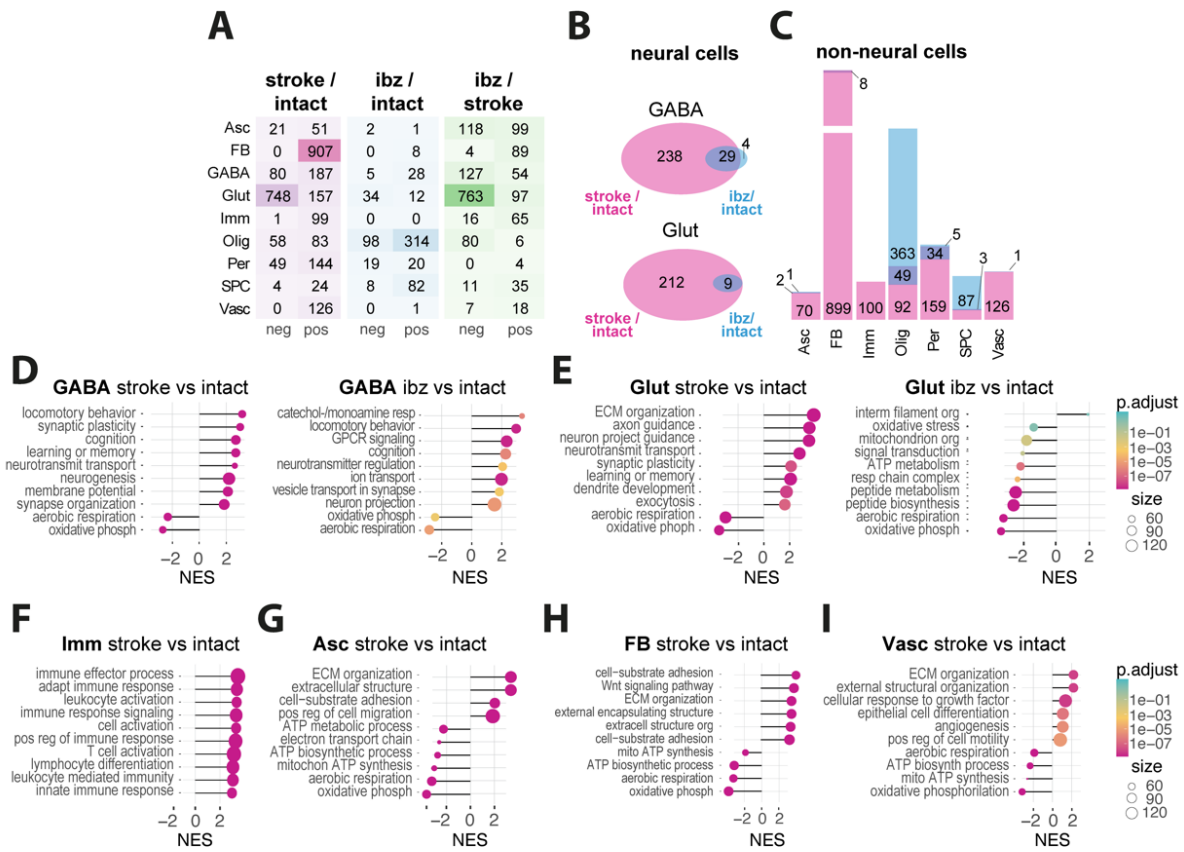
Fig 2: Comparative analysis of transcriptomic responses in mouse and human stroke. (A) Heatmap showing number of significantly up- and downregulated genes per cell types in stroke vs intact (left), ibz vs intact (middle) and ibz vs stroke (right) tissue. (B) Venn diagram showing the overlap and unique differentially expressed genes from neural cells between stroke and ibz tissue (C) Bar plot showing the common and differential expressed genes in non-neural cells (right). (D-I) Gene set enrichment analysis (GSEA) of biological pathways that are enriched in stroke vs intact and ibz vs intact tissue for (D) GABA, (E) Glut, and GSEA from stroke vs intact tissue in (F) Imm, (G) Asc, (H) FB, and (I) Vasc. Each panel displays the normalized enrichment score (NES) for pathways that are overrepresented (positive NES) or underrepresented (negative NES) in the post-stroke environment compared to intact tissue.

Mapping of intercellular molecular communication after stroke

To quantitatively infer and identify relevant communication networks after stroke, we used CellChat[43,44] to analyze signaling patterns involved in ligand-receptor interactions between individual cell types (**Fig 3A**). Our analysis suggests that the total number and strength of predicted interactions are increased in stroke tissue (**Fig 3B, C**; number of interactions: stroke / intact: +104%, stroke / ibz: +71%: interaction strength: stroke / intact: +95%; ibz / intact+104%).

In stroke-injured tissue, we observed an upregulation of interactions among individual cell types (**Fig 3C**), with the majority of communication occurring between information sending Glut, GABA, Asc, IC and FB and information receiving Glut, GABA and Asc (**Fig. 3D**). By contrast, cells derived from the ibz and intact tissue exhibited a lower number of predicted interactions especially among non-neural cell populations such as Imm, Vasc, Per, IC and Olig compared to corresponding cell types from stroke-injured tissue (**Fig 3D, E**). In stroke-affected tissue, Glut and Asc, particularly as senders, display significantly increased interactions, with IC also showing heightened communication compared to intact tissue. Conversely, in the ibz, these interactions are less pronounced, with non-neural cells like Imm and Vasc cells engaging in fewer communications overall. The data suggests a substantial upregulation of neural cell interactions post-stroke, with a notable contribution from IC cells in stroke conditions (**Fig 3E**).

To better understand the involved signaling pathways in stroke compared to intact tissue, we grouped and clustered signaling pathways in four groups separated by functional similarity (**Fig 3F**). Most divergent pathways were linked with important biological functions such as neuronal guidance and plasticity (SEMA3, SEMA7, UNC5, SLIT, EPHA), vascular repair and ECM remodeling (COLLAGEN, LAMININ, CDH, CADM, ANGPT, FGF, MMP9).

Most of these pathways demonstrated a considerably higher information flow in stroke-injured tissue (**Fig 3G, H**). For instance, stroke tissue showed enhanced communication via the COLLAGEN, PTPR, PTN, NEGR, LAMININ, CNTN and CADM pathways, involving multiple cell types that either did not participate or exhibited only minimal signaling interactions in intact tissue (**Fig 3I**). Interactions of individual cell types in these pathways reveals that ICs preferentially signal to non-neural cells through networks related to COLLAGEN and LAMININ networks involving e.g., Col1a2, Col1a1, Lama2. These signals are predicted to be received by astrocytes (e.g., Itgav-Itgb8), fibroblasts (itga1-itgb1, Ptgdr) and vascular cells (Itga1-itgb1, Itga6-itgb1). This signaling pattern appears to be distinct from the signaling of other non-neural cells such as fibroblasts (e.g. App), astrocytes (e.g., Sema6a, Sema4d, Angpt1) and pericytes (e.g., Lama2) (**Fig 3J**).

Overall, these findings show the surprisingly complex and dynamic communication among individual cell types in stroke-injured brains.
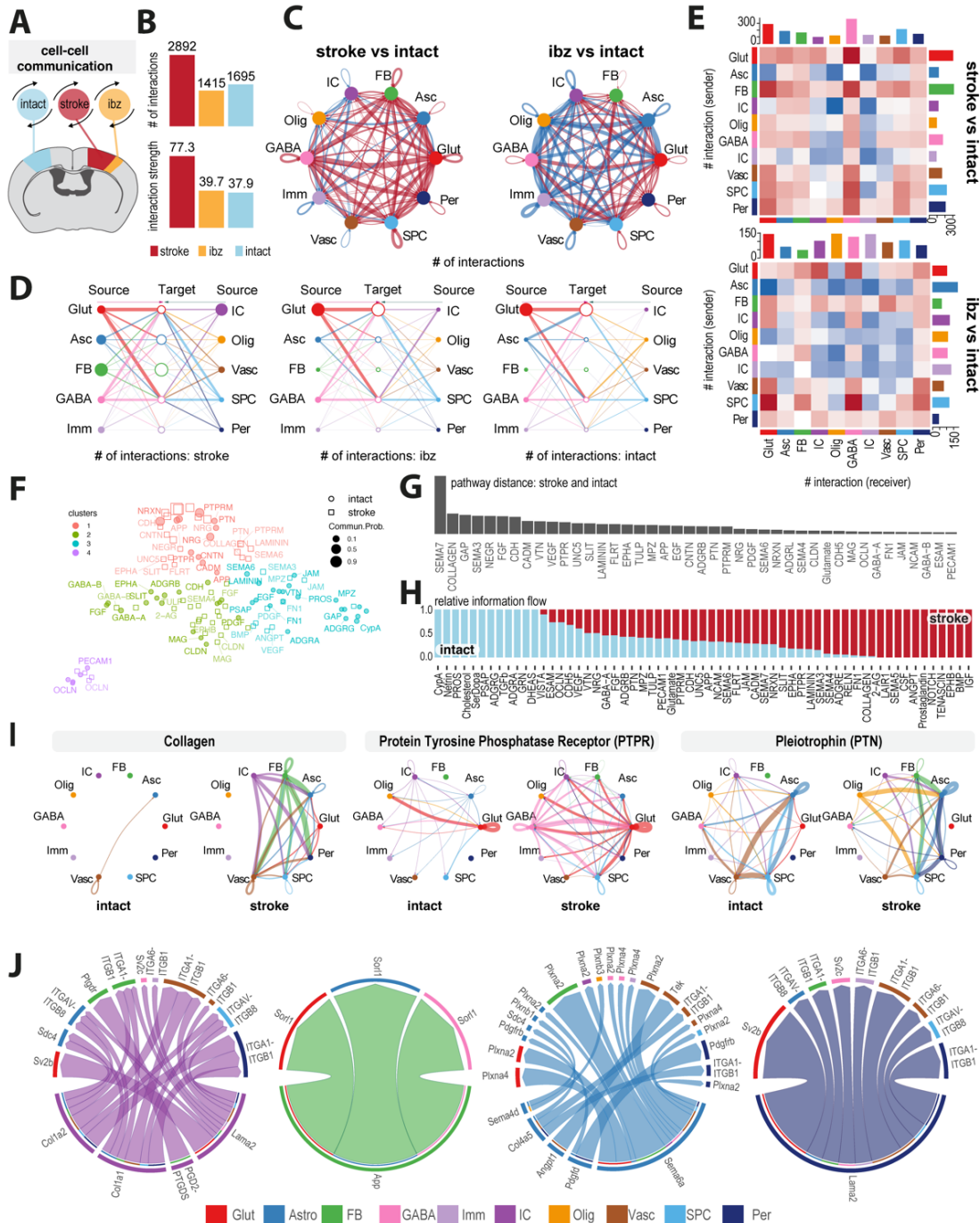
Fig 3: Mapping of intercellular molecular signaling post-stroke. (A) Schematic of cell-cell interaction analysis (B) Bar plot showing number and strength of interactions in cells from intact, ibz and stroke tissue. (C) Network diagram contrasting total number of cell-cell interactions between individual cell types in stroke vs intact (left) and ibz vs intact (right). Red lines indicate increased interaction, blue lines indicate reduced interaction, relative to intact tissue. (D) Hierarchy plot of interaction between all individual cell types to target cells in stroke (left), ibz (middle) and intact (right) datasets. (E) Heatmap showing differential interactions between cell types from stroke vs intact (upper) and ibz vs intact tissue (lower). Red squares indicating increased signaling and blue squared indicating decreased signaling, relative to cells from intact tissue. (F) Scatter plot projecting signaling groups onto a 2D space according to their functional similarity between cells from stroke and intact tissue. (G) Bar plot showing signaling pathway distance between stroke and intact tissue (H) Stacked bar plot illustrating the proportional relative information flow in signaling pathways between intact and stroke tissue. (I) Cell-cell communication networks for selected pathways: COLLAGEN, Protein Tyrosine Phosphatase Receptor (PTPR), and Pleiotrophin (PTN) across cell types in intact (left) and stroke (right) tissue. (J) Chord diagrams showing the most upregulated signaling ligand-receptor pairings in injury-associated cells (IC), fibroblasts (FB), astrocytes (Asc), and pericytes (Per).

Comparative analysis of transcriptome responses in mouse and human stroke

To decode and highlight transcriptomic changes that may be relevant to human stroke, we compared our mouse pseudo-bulk and ortholog-transformed RNAseq data with publicly available human stroke-lesion RNAseq datasets from cortical lesions and contralesional brain tissue of patients who experienced a nonfatal ischemic stroke up to five years before death (GSE56267)[45] (**Fig 4A**).

We performed a Pearson correlation analysis of the genes shared by mouse and human datasets post-stroke, which revealed similarities in gene expression changes (r = 0.43, p < 0.001) (**Fig 4B**). Interestingly, we found that IGFBP5, previously identified as upregulated in IC cells of stroke mice, was also upregulated in the human stroke dataset (**Fig 4B**). We then calculated z-scores of log2-fold changes and revealed shared and differentially expressed genes between the mouse and human datasets (**Fig 4C**). The overlapping upregulated gene expression featured genes associated with inflammation (e.g., CXCL5, CD44, CD36), neural plasticity (e.g., GAP43, RUNX1), ECM remodeling (e.g., ADAM12, MMP2, COL4A6) and vascular remodeling (e.g., ANGPTL4, CLDN5).

We observed that 48% of the top 2000 genes, 22% of the top 500 genes, and 4% of the top 100 genes were commonly upregulated in both mouse and human post-stroke. Moreover, of the 861 human genes exhibiting more than a 2-fold upregulation following stroke, 717 (83%) were also upregulated in the mouse stroke dataset (**Fig 4D**).

We then conducted an over-representation analysis (ORA) of biological processes among the top 2000 upregulated genes that were (a) common: upregulated in mouse and human, (b) mouse-specific, and (c) human-specific. The common ORA predominately featured inflammation-related pathways including regulation of cytokines and immune cells activation, along with angiogenesis, ECM regulation and wound healing responses (**Fig 4E**; all p < 0.001).

Mouse-specific ORAs similarly highlighted pathways of inflammation, wound healing, and gliogenesis (**Fig 4F**; all p < 0.001). In contrast, human-specific ORAs were primarily associated with pathways involved in cell division and structural organization (**Fig 4G**; all p < 0.001), potentially highlighting species-specific differences in the cellular repair mechanisms post-stroke.

In summary, our analysis underscores the substantial cross-species similarities in stroke-induced transcriptomic changes, especially in key pathways related to inflammation and tissue remodeling, highlighting conserved biological mechanisms that could inform the development of therapeutic strategies for human stroke recovery.
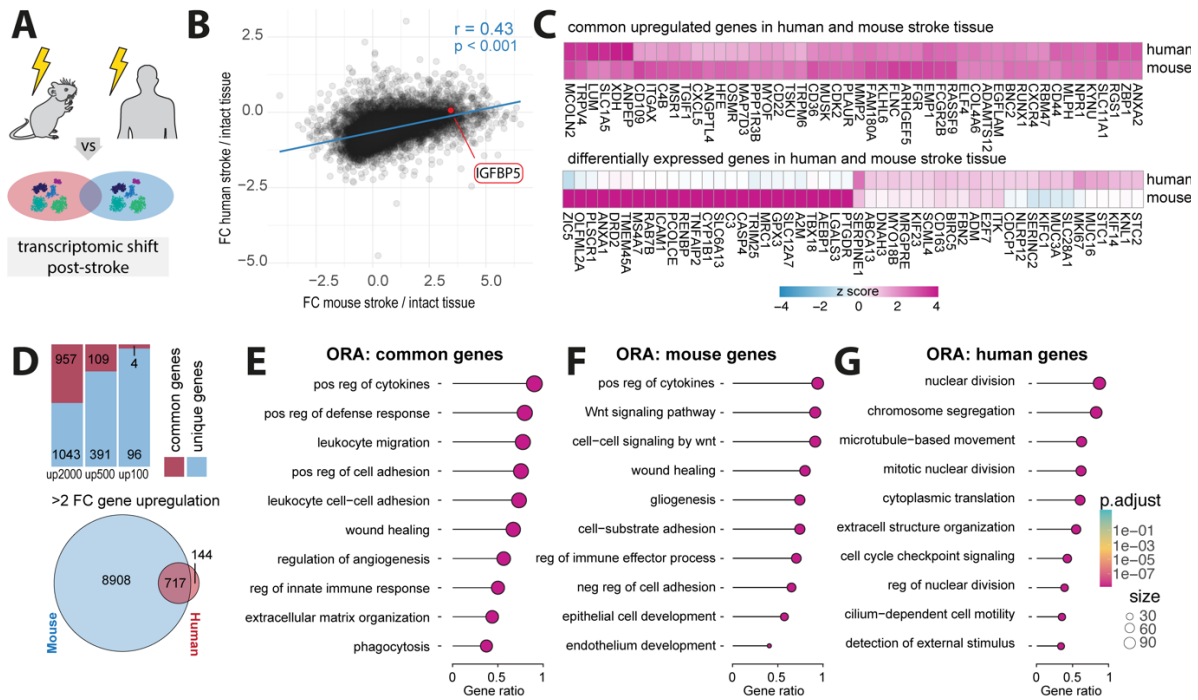
Fig 4: Comparative gene expression profiles in mouse and human post-stroke. (A) Schematic of human and mouse stroke (B) Scatter plot displaying the Person correlation for gene expression changes between mouse and human post-stroke. (C) Heatmap of common upregulated genes in human and mouse stroke (upper) and differentially expressed genes in human and mouse stroke (lower) (D) Stacked barplot of common and unique upregulated genes in the top 2000, 500 and 100 gene sets from both mouse and human datasets (upper) and Venn diagram of shared and unique genes with a fold change >2. (E-G) Overrepresentation analysis of top 2000 genes present in (E) both mouse and human datasets, (F) genes exclusively identified in mouse stroke dataset (G) and genes only present in human stroke dataset. All p-values ***,< 0.001.

Discussion

278

279　　　In this study, we have provided a resource for exploring single-cell transcriptomic data
280　from distinct brain areas one month after stroke injury. Understanding the transcriptomic shifts
281　of individual brain cells and the intracellular signaling mechanisms involved may further help
282　to identify novel therapeutic targets. Our comparative analysis to human chronic stroke dataset
283　has shown a considerable overlap in molecular gene and pathway enrichment suggesting
284　similarities in the pathophysiology of chronic stroke between mice and humans.

285　　　We observed a strong reduction of GABAergic and glutamatergic neurons one month
286　following stroke within the injury core and peri-infarct areas. Interestingly, gene expression
287　profiles of the surviving cells, irrespective of their type, indicated a downregulation of genes
288　involved in aerobic metabolism, implying a state of persistent hypoxia within the stroke
289　regions. This observation aligns with previous studies that have documented prolonged
290　alterations in cerebral blood flow post-stroke in both murine models and human patients[46,47].
291　While all neurons mainly rely on aerobic metabolism[48], neurons with especially high energy
292　demands, such as glutamatergic pyramidal neurons and fast-spiking GABAergic neurons
293　(e.g., PV-expressing interneurons), may be even more susceptible to hypoxia[36].

294　　　Our findings indicate a considerable reduction in the glutamatergic and GABAergic
295　neurons, which has been previously shown to affect stroke recovery[35,49]. In glutamatergic
296　neurons, we observed upregulation of axon guidance and synaptic organization pathways,
297　partially mediated through semaphorin (Sema) signaling. Plexin D1–Sema3e receptor-ligand
298　interaction has been implicated in controlling synapse formation and affecting post-stroke
299　recovery[50,51]. Various studies have reported an increase of guidance factors, including
300　Sema3e after stroke[30,52,53]. There is evidence suggesting that blockage of Sema3e/PlexinD1
301　pathway might offer therapeutic benefits for restoring function after stroke[41]. However, other
302　findings indicate that genetic deletion of PlexinD1 signaling can lead to impairments in the
303　BBB[52].

304　　　In our study, we observed a pronounced upregulation of genes and pathways
305　associated with ECM remodeling in non-neural cells including astrocytes, fibroblasts, and
306　vascular cells. This upregulation is consistent with the well-known formation of a fibrotic scar
307　in the stroke core, closely bordered by a glial scar after stroke. Importantly, we observed the
308　ECM remodeling molecular signature in multiple non-neural cell types within the stroke,
309　supporting the previously described cellular composition of the scar including ECM-producing
310　PDGFRβ+ stromal fibroblasts, pericytes, reactive astrocytes, microglia, and monocyte-derived
311　macrophages[54]. While the glial scar has been known for its dual role, potentially protecting the
312　brain from further damage[55–57], the fibrotic scar is primarily regarded as detrimental,

313   particularly due to its inhibitory effect on regeneration[54,58]. Through cell-cell communication

314   networks, we predicted that most upregulated signaling pathways include major components

315   of ECM remodeling including collagen, integrin, and laminin pathways in multiple non-neural

316   cells. Several integrin subunits α1β1, αvβ3, and α6β1 have been shown to regulate vascular

317   remodeling and attenuate BBB permeability following stroke[59–61]. Several integrin subtypes

318   have also been described to be involved in astrocyte scar formation and the phenotypic switch

319   of astrocytes[62–64]. Notably, certain integrins, such as αIIbβ3, α4β7/α4β1, and αLβ2, are

320   druggable targets that have been explored in cardiovascular diseases and inflammatory bowel

321   disease[65]. Future research therefore may explore integrin-targeted therapies in stroke.

322   We identified a cell cluster of cells, termed 'injury associated cells' (IC) in the stroke

323   core that was barely present in peri-infarct nor intact tissue. There is evidence suggesting that

324   ICs may be fibroblast-like cells that migrate to injury sites after stroke. However, their

325   molecular characterization is challenging since there are only few fibroblast-specific markers

326   and many of those markers can be substantially altered after injury[66]. For instance, we

327   observed presence of Col1α1 and Vim, markers that have been used to identify fibroblasts,

328   however, those markers can also be found on other cell types such as activated astrocytes[67,68]

329   or injury-associated pericyte-like cells (type A pericytes)[69]. The function of Col1α1+ associated

330   cells in the injured brain has been described as both neuroprotective and detrimental.[63,64]

331   Studies have shown that Col1α1+ fibroblast-like cells are a crucial source of retinoic acid,

332   promoting neural progenitor differentiation and improving recovery in rodent stroke models[69].

333   Furthermore, research on chronic mouse ischemic stroke models reveals that Col1^{+}

334   fibroblast-like cells in peri-infarct areas strongly express periostin, which has been linked to

335   improved recovery in neonatal hypoxic-ischemic mice by promoting neural stem cell

336   proliferation and differentiation[70]. On the other hand, blocking PDGFRα, which is expressed

337   in fibroblast-like cells has been shown to preserve the BBB[71]. The origin of Col1α1[+] fibroblast-

338   like cells remains unknown, though some evidence suggests a potential pericyte origin[72].

339   These cells likely represent a heterogeneous group of fibroblasts, possibly including cells

340   derived from diverse sources such as dural, arachnoid, pial, and perivascular fibroblasts, as

341   well as meningothelial cells with distinct properties and functions in stroke. Recent single-cell

342   transcriptomic studies help us to understand the complex diversity of fibroblasts in

343   developmental and adult brain tissue[73,74], and future research on stroke tissue could further

344   reveal the unique characteristics of Col1α1+ fibroblast-like cells. Moreover, ICs were identified

345   to express insulin-like growth factor-binding protein 5 (IGFBP5). Additional immunostaining of

346   stroked and intact brain sections revealed upregulation of IGFBP5 in the stroke core,

347   compared to peri-infarct nor the intact tissue. We also found upregulation of IGFBP5 in the

348   analyzed human stroke dataset. IGFBP5, the most conserved member of the IGFBP family,

349   plays various biological roles, such as influencing the inflammatory response[75], fibrosis[76], cell

350   adhesion[77], and cell migration and proliferation[78]. Recent research shows that IGFBP-5 has

351   specific roles depending on the cell type and the physiological or pathological context. It may

352   be involved in the development of atherosclerosis by binding to extracellular matrix (ECM)

353   components PAI-1 and osteopontin, which are found in atherosclerotic plaques and have been

354   shown to promote atherosclerosis in loss-of-function studies[79–81]. *In vitro* studies with primary

355   human idiopathic pulmonary fibrosis (IPF) fibroblasts have shown that both exogenous and

356   endogenously expressed IGFBP-5 increase the expression of ECM component-associated

357   genes and pro-fibrotic genes[82]. Recent findings also suggest that IGFBP5 is essential for

358   regulating angiogenesis. IGFBP5 is induced during reparative angiogenesis in a hind limb

359   ischemia model, and blocking of IGFBP5 has been shown to enhance angiogenesis by

360   boosting ATP metabolism and stabilizing HIF1α via E3 ubiquitin ligase VHL[83]. These results

361   suggest that IGFBP5 could be an interesting pharmacological target for treating conditions

362   related to impaired angiogenesis, such as stroke.[84]

363   Our comparative analysis of transcriptomic changes in human and mouse stroke tissue

364   revealed a shared upregulation of genes and pathways, indicative of a conserved response to

365   stroke across species. This analysis has highlighted key genes like CXCL5 and C4B, which

366   are involved in the inflammatory response, suggesting an orchestrated immune activation in

367   the chronic phase of stroke. CXCL5 has been reported as a potential CSF biomarker

368   correlating with brain damage in stroke patients[85], but also beyond the acute phase patients

369   exhibit a proinflammatory signature after stroke. Elevated CXCL5 proteins have been reported

370   in blood from stroke patients up to 7 years after injury[86]. Another shared pathway was ECM

371   remodeling involving genes such as MMP2 and COL4. Alterations in COL4 expression after

372   stroke have been described in rodent models of MCAO and non-human primates[87,88].

373   Furthermore, an association between Col4 mutations and ischemic stroke has been described

374   in humans, suggesting that Collagen IV plays an important role in the pathogenesis and

375   recovery of ischemic stroke in both species[89].

376   The upregulation of ANGPTL4 suggests the role of angiogenesis in post-stroke

377   recovery. Post-stroke angiogenesis has been reported as an important recovery in

378   experimental and human stroke[30,90–92]. More recently, ANGPTL4 was associated with poor

379   prognosis in acute ischemic stroke patients[93]. The cross-species comparison enhances the

380   validity of these findings and suggests that druggable pathways that show beneficial effects in

381   the mouse may target the same pathway in chronic human stroke.

382   We recognize that our molecular stroke atlas is only a first step towards deciphering the

383   molecular and cellular interaction following a stroke. We acknowledge limitations such as

384   unintended biases in nuclei isolation and tissue collection from stroke-affected, peri-infarct,

385   and intact tissue, of each mouse. These biases might affect the relative cell proportions and

386   will require future validation using spatially resolved datasets. Additional work should extend

387   to validating our findings in longer-term studies, beyond one month, and in alternative stroke

388   models such as the permanent and transient middle cerebral artery occlusion (pMCAo)

389   models in rodents, non-human primates, and human stroke patients. Despite these limitations,

390   our results offer valuable insights for upcoming research into the long-term mechanisms of

391   stroke pathology and the development of therapeutic strategies.

Materials and Methods

392

393   Experimental design:

394   The study was designed to generate a single-cell atlas of stroke-injured mouse tissue one
395   month following permanent focal cerebral stroke. we used nine stroked adult male and female
396   mice (3-5 months old) with a C57BL/6J background. We validated a successful stroke
397   induction using Laser Doppler imaging and collected tissue from stroke, peri-infarct and intact
398   cortex. We dissociated the tissue and isolated nuclei for subsequent snRNAseq analysis. We
399   compared the mouse transcriptome with a publicly available human stroke dataset
400   (GSE56267).

401

402   Photothrombotic stroke induction:

403   Photothrombotic stroke was induced as previously described [32,94–96]. Briefly, anesthesia was
404   induced with 4% isoflurane delivered in oxygen. When their respiration rate reached
405   approximately 50 breaths per minute, indicating deep anesthesia, they were placed into a
406   stereotactic frame (Davids Kopf Instruments). A custom-made face mask provided a steady
407   supply of 1-2% isoflurane. Their body temperature was regulated at 36-37 °C using a heating
408   pad. The absence of the toe pinch reflex confirmed deep anesthesia, and Vitamin A eye
409   lubricant from Bausch&Lomb was applied to prevent eye dryness during the procedure. The
410   head was shaved from the neck to the snout, sanitized and Emla™ Creme 5% was applied to
411   the scalp and ears. Ear bars were then inserted to stabilize the head. A 1 cm incision was
412   made to expose the Lambda and Bregma, which were cleaned using a Q-tip. The stroke
413   induction site was precisely marked using an Olympus SZ61 surgery microscope and a WPI
414   UMP3T-1 stereotactic coordinate system, taking Bregma as the reference. Rose Bengal in
415   0.9% NaCl solution at 15mg/ml was injected intraperitoneally at a dose of 10µl/g bodyweight
416   5 minutes before a 150W, 3000K Olympus KL1500LCD cold light source was used for
417   illumination at the marked site for 10 minutes. After the procedure, animals were placed in a
418   recovery cage.

419

420   Laser Doppler imaging (LDI):

421   After stroke induction, anesthetized mice were secured in a stereotactic apparatus. The mice
422   underwent a single-point Laser Doppler Imaging (LDI) procedure using the Moor Instruments
423   MOORLDI2-IR device. LDI data was then extracted and the total flux within the region of
424   interest (ROI) was measured using Fiji (ImageJ). Subsequent analysis was carried out using
425   R software.

426 Tissue processing:

427 For RNA sequencing, animals were perfused transcardially on ice using Ringer's solution
428 (0.9% NaCl). Subsequently, the specified cortical brain tissue was rapidly dissected on ice
429 with the assistance of a microbiopsy instrument (Kai Medical) and a stereotaxic microscope
430 (Olympus). The collected tissue was then immediately frozen in liquid nitrogen. For
431 immunohistochemistry, perfusion was performed using Ringer's solution (0.9% NaCl),
432 followed by a perfusion with a 4% paraformaldehyde (PFA) solution. The brain was extracted
433 and post-fixed for 6 hours in 4% PFA. The brains were stored in 0.1 M PBS. Before
434 immunohistochemistry, the brains were sectioned into 40 μm coronal slices using a Thermo
435 Scientific HM 450 sliding microtome. Next, brain sections were rinsed with 0.1 M PBS. They
436 were then treated with 500 μl of blocking buffer (5% donkey serum in 1x PBS with 0.1% Triton®
437 X-100) and incubated for 1 hour at room temperature. Following blocking, the sections were
438 incubated with primary antibodies (Table 1) on an Unimax 1010 shaker set to approximately
439 90 rpm, and this was maintained overnight at 4°C. The next day, after washing, the sections
440 were incubated with appropriate secondary antibodies (Table 2), for 2 hours at room
441 temperature. Additionally, the sections were treated with DAPI (Sigma, diluted 1:2000 in 0.1
442 M PBS) to stain the nuclei. Finally, the sections were arranged on Superfrost Plus™
443 microscope slides, immersed in Mowiol® mounting medium, and securely coverslipped.

444

445 *Table 1: Primary Antibody List.*

Antigen	Target	Host	Dilution	Company
CD13	Pericytes	goat	1:200	R&D Systems
CD31	Vascular endothelial cells	rat	1:50	BD Biosciences
GFAP	Astrocytes	mouse	1:200	R&D Systems
Iba1	Microglia	goat	1:200	R&D Systems
CD68	Macrophages	rat	1:200	BioLegend
vGlut1	Glutamate transporter in synaptic vesicles	mouse	1:300	Synaptic Systems
GAT1	GABA transporter in synaptic vesicles	rabbit	1:200	Abcam
IGFBP5	Insulin-like growth factor-binding protein 5	rabbit	1:100	Proteintech
NeuN	Neurons	rat	1:200	Abcam

446

447 *Table 2: Secondary Antibody List.*

Reactivity	Host	Conjugate	Dilution	Company
anti-rabbit	Donkey	Cy5	1:100	*Jackson*
anti-rat	Donkey	Cy3	1:500	*Jackson*
anti-goat	Donkey	AlexaFluor 488	1:500	*Jackson*
anti-mouse	Donkey	Cy3	1:500	*Jackson*
anti-rabbit	Donkey	AlexaFluor 488	1:500	*Jackson*

Anti-mouse	Donkey	AlexaFluor 488	1:500	*Jackson*
Anti-goat	Donkey	Cy3	1:500	*Jackson*
Anti-rabbit	Donkey	AF647	1:100	*Jackson*

448

449   Isolation of nuclei from frozen brains:

450   Nuclei were extracted from frozen cortical brain tissues as previously described[97]. Tissues
451   were rapidly frozen in liquid nitrogen and subsequently pulverized using a Dounce
452   homogenizer in a lysis solution composed of 10 mM Tris-HCl (pH 7.5), 10 mM NaCl, 3 mM
453   MgCl2, and 0.1% Nonidet P40 dissolved in nuclease-free water. After a 15-minute incubation,
454   the homogenate was strained through a 30 μm cell strainer. The strained suspension was then
455   subjected to a low-speed centrifugation at 500g for 5 minutes at 4°C to sediment the nuclei.
456   These nuclei were washed and passed through a 40 μm cell strainer twice, using sterile PBS
457   supplemented with 2% BSA and 0.2 U/μl RNase inhibitor. The nuclei were then suspended in
458   500 μl of the washing buffer and combined with 900 μl of 1.8 M sucrose solution. This mixture
459   was carefully overlaid onto 500 μl of 1.8 M sucrose and centrifuged at 13,000g for 45 minutes
460   at 4°C, facilitating myelin removal. The final pellet was resuspended in the washing buffer and
461   filtered once more through a 40 μm cell strainer to ensure purity.

462

463   Single-nucleus RNA sequencing:

464   Single-nucleus RNA sequencing (snRNAseq) was performed as previously described.[97] For
465   the droplet-based library construction, nuclei isolated from both stroked and non-stroked
466   mouse cortices were processed on the Chromium system by 10x Genomics, following the
467   manufacture's guidelines. RNA capture and subsequent amplification were facilitated by the
468   Chromium Single Cell 3' Reagent Kits v3. Sequencing of the resulting libraries was executed
469   on an Illumina sequencing platform. The analysis pipeline, including demultiplexing of
470   samples, processing of barcodes, and enumeration of single cells, was conducted using the
471   Cell Ranger Single-Cell Software Suite supplied by 10x Genomics.

472

473   Clustering and annotation cell types:

474   For the clustering and annotation of cell types, single-nucleus RNA sequencing (snRNAseq)
475   data alignment and gene quantification were performed using Cellranger v3.1.0, which
476   followed default settings and referenced the mm10 2020-A dataset. Cells were screened,
477   excluding any with greater than 5% mitochondrial gene expression or with less than 500
478   nFeature_RNA. Normalization and scaling of gene counts were performed using Seurat
479   v5.0.192, to adjust for total unique molecular identifier counts per cell. Using the initial 30
480   principal components, cell clustering was accomplished via the FindNeighbors function, with

481   subsequent clustering by the FindClusters function. Dimensionality was reduced through

482   Uniform Manifold Approximation and Projection (UMAP) employing the RunUMAP function.

483   Distinct cell types were identified based on established markers, categorizing into

484   Glutamatergic neurons (Glut: e.g., Slc17a7, Satb2), GABAergic neurons (GABA: e.g., Gad1,

485   Gad2), Astrocytes (Asc: Slc1a2, Slc1a3), Fibroblasts (FB: Col1a, Fn1), Oligodendrocytes

486   (Olig: Mbp, Plp1), Immune cells (IC: Inpp5d, Csf1r), vascular cells (Vasc: Flt1, Cldn5), stem

487   and progenitor cells (SPC: Sox10, Vcan), and mural cells (Per: Pdgfrb Cspg4). The cell types

488   and marker expression of cell types matched sc/snRNAseq datasets[12,26,27]. FindMarkers

489   function was used to pinpoint cell type–specific marker genes, considering genes with a

490   Bonferroni correction adjusted P value <0.05 as significant markers. The downstream analysis

491   (including Gene Set Enrichment analysis (GSEA), and over representation analysis (ORA)

492   was performed using R package ClusterProfiler.

493

494   Cell-cell communication with CellChat:

495   Differential cell-cell interaction networks were generated using CellChat version 2.1.0[43,44]. In

496   brief, DifferentialConnectome was applied to the Seurat objects (version 5.01), which

497   contained integrated data of mouse stroke, ibz and intact datasets. The compareInteractions

498   function was utilized to compute the total number of interactions and their strengths, while

499   network centrality was scored using the netAnalysis_computeCentrality function. All analyses

500   were conducted in line with the 'Full tutorial for CellChat analysis of a single dataset with

501   detailed explanation of each function' found on the GitHub page.

502

503   Human RNAseq dataset:

504   Human stroke RNA sequencing data was obtained from the NCBI Gene Expression Omnibus,

505   accession number GSE56267. For the purpose of comparing differential gene expression

506   profiles between mouse and human stroke, we employed a pseudo-bulk approach on the

507   mouse snRNAseq data using the AggregateExpression() function in the Seurat package. We

508   processed both datasets using Z-score normalization and translated mouse gene identifiers

509   to their human orthologs. To evaluate the relationship between gene expression in mouse and

510   human stroke cases, Pearson's correlation test was used. Subsequent analyses, which

511   included Gene Set Enrichment Analysis (GSEA) and Over Representation Analysis (ORA),

512   were conducted using the ClusterProfiler package in R, providing comprehensive insights into

513   the biological significance of the expression data.

514

515   Statistical analysis:

516   Statistical analysis was performed using RStudio (Version 4.04). Sample sizes were designed

517   with adequate power in line with previous studies from our group[98–100] and relevant literature.

518   One-way analyses of variance (ANOVA) followed by Tukey multiple comparison test was

519   performed for cerebral blood flow measurements. The assumption of normality was tested by

520   Kolmogorov–Smirnov tests and by inspecting residuals with QQ plots. Data is expressed as

521   mean ±SD; statistical significance was defined as $*p < 0.05$, $**p < 0.01$, and $***p < 0.001$.

522

523   Data availability:

524   Raw single nucleus RNA sequencing data was deposited in the NCBI Gene Expression

525   Omnibus (GEO) and will be available following publication. Data are now also available to

526   explore via an interactive web browser: https://rustlab.shinyapps.io/Stroke-Atlas/

527

Competing Interest Statement

The authors declare that the research was conducted in the absence of any commercial or financial relationships that could be construed as a potential conflict of interest.

Author contribution

RZW, CT, BVZ, RR contributed to overall project design. RZW, KK, BVZ, RR contributed to the design of snRNAseq experiments. RZW, BAB, NHR, RR conducted and analyzed *in vivo* experiments. RZW, AB, MZ, RR performed nuclei isolation and snRNAseq experiments. RR analyzed snRNAseq experiments. RZW, RR made figures. BVZ, CT, RR supervised the study. RZW, KK, BVZ, CT, RR wrote and edited the manuscript with input from all authors. All authors read and approved the final manuscript.

References

1. Tsao, C. W. *et al.* Heart Disease and Stroke Statistics-2023 Update: A Report From the American Heart Association. *Circulation* **147**, e93–e621 (2023).

2. Feigin, V. L. *et al.* Global, regional, and national burden of stroke and its risk factors, 1990–2019: a systematic analysis for the Global Burden of Disease Study 2019. *The Lancet Neurology* **20**, 795–820 (2021).

3. Rust, R. *et al.* Brain repair mechanisms after cell therapy for stroke. *Brain* awae204 (2024) doi:10.1093/brain/awae204.

4. Dias, D. O. *et al.* Pericyte-derived fibrotic scarring is conserved across diverse central nervous system lesions. *bioRxiv* 2020.04.30.068965 (2020) doi:10.1101/2020.04.30.068965.

5. Zamboni, M., Llorens-Bobadilla, E., Magnusson, J. P. & Frisén, J. A Widespread Neurogenic Potential of Neocortical Astrocytes Is Induced by Injury. *Cell Stem Cell* **27**, 605-617.e5 (2020).

6. Bellver-Landete, V. *et al.* Microglia are an essential component of the neuroprotective scar that forms after spinal cord injury. *Nat Commun* **10**, 518 (2019).

7. Gu, Y. *et al.* Conditional ablation of reactive astrocytes to dissect their roles in spinal cord injury and repair. *Brain Behav Immun* **80**, 394–405 (2019).

8. Almanzar, N. *et al.* A single-cell transcriptomic atlas characterizes ageing tissues in the mouse. *Nature* **583**, 590–595 (2020).

9. Callaway, E. M. *et al.* A multimodal cell census and atlas of the mammalian primary motor cortex. *Nature* **598**, 86–102 (2021).

10. Hahn, O. *et al.* Atlas of the aging mouse brain reveals white matter as vulnerable foci. *Cell* **186**, 4117-4133.e22 (2023).

11. Winkler, E. A. *et al.* A single-cell atlas of the normal and malformed human brain vasculature. *Science* **375**, eabi7377 (2022).

12. Yao, Z. *et al.* A high-resolution transcriptomic and spatial atlas of cell types in the whole mouse brain. *Nature* **624**, 317–332 (2023).

13. Hardwick, S. A. *et al.* Single-nuclei isoform RNA sequencing unlocks barcoded exon connectivity in frozen brain tissue. *Nat Biotechnol* **40**, 1082–1092 (2022).

14. Bakken, T. E. *et al.* Comparative cellular analysis of motor cortex in human, marmoset and mouse. *Nature* **598**, 111–119 (2021).

15. Yang, A. C. *et al.* A human brain vascular atlas reveals diverse mediators of Alzheimer's risk. *Nature* **603**, 885–892 (2022).

16. Garcia, F. J. *et al.* Single-cell dissection of the human brain vasculature. *Nature* **603**, 893–899 (2022).

17. Mathys, H. *et al.* Single-cell atlas reveals correlates of high cognitive function, dementia, and resilience to Alzheimer's disease pathology. *Cell* **186**, 4365-4385.e27 (2023).

18. Garcia-Bonilla, L. *et al.* Analysis of brain and blood single-cell transcriptomics in acute and subacute phases after experimental stroke. *Nat Immunol* 1–14 (2024) doi:10.1038/s41590-023-01711-x.

19. Callegari, K. *et al.* Molecular profiling of the stroke-induced alterations in the cerebral microvasculature reveals promising therapeutic candidates. *Proceedings of the National Academy of Sciences* **120**, e2205786120 (2023).

20. Matson, K. J. E. *et al.* Single cell atlas of spinal cord injury in mice reveals a pro-regenerative signature in spinocerebellar neurons. *Nat Commun* **13**, 5628 (2022).

21. Rust, R. Ischemic stroke-related gene expression profiles across species: a meta-analysis. *J Inflamm* **20**, 21 (2023).

22. Buizza, C., Enström, A., Carlsson, R. & Paul, G. The Transcriptional Landscape of Pericytes in Acute Ischemic Stroke. *Transl. Stroke Res.* (2023) doi:10.1007/s12975-023-01169-x.

23. Beuker, C. *et al.* Stroke induces disease-specific myeloid cells in the brain parenchyma and pia. *Nat Commun* **13**, 945 (2022).

24. Nakahashi-Oda, C. *et al.* CD300a blockade enhances efferocytosis by infiltrating myeloid cells and ameliorates neuronal deficit after ischemic stroke. *Science Immunology* **6**, eabe7915 (2021).

25. Barisano, G. *et al.* A "multi-omics" analysis of blood–brain barrier and synaptic dysfunction in APOE4 mice. *Journal of Experimental Medicine* **219**, e20221137 (2022).

26. Yao, Z. *et al.* A taxonomy of transcriptomic cell types across the isocortex and hippocampal formation. *Cell* **184**, 3222-3241.e26 (2021).

27. Yao, Z. *et al.* A transcriptomic and epigenomic cell atlas of the mouse primary motor cortex. *Nature* **598**, 103–110 (2021).

28. Chistiakov, D. A., Killingsworth, M. C., Myasoedova, V. A., Orekhov, A. N. & Bobryshev, Y. V. CD68/macrosialin: not just a histochemical marker. *Lab Invest* **97**, 4–13 (2017).

29. Nguyen, J. N. *et al.* CD13 facilitates immune cell migration and aggravates acute injury but promotes chronic post-stroke recovery. *J Neuroinflammation* **20**, 232 (2023).

30. Rust, R. *et al.* Nogo-A targeted therapy promotes vascular repair and functional recovery following stroke. *Proc Natl Acad Sci USA* 201905309 (2019) doi:10.1073/pnas.1905309116.

31. Rust, R. *et al.* Anti-Nogo-A antibodies prevent vascular leakage and act as pro-angiogenic factors following stroke. *Sci Rep* **9**, 1–10 (2019).

32. Weber, R. Z. *et al.* Characterization of the blood brain barrier disruption in the photothrombotic stroke model. *Front. Physiol.* (2020).

33. Rust, R. *et al.* A Practical Guide to the Automated Analysis of Vascular Growth, Maturation and Injury in the Brain. *Front. Neurosci.* **14**, (2020).

34. Motaharinia, M. *et al.* Longitudinal functional imaging of VIP interneurons reveals sup-population specific effects of stroke that are rescued with chemogenetic therapy. *Nat Commun* **12**, 6112 (2021).

35. Xie, Y., Chen, S., Wu, Y. & Murphy, T. H. Prolonged Deficits in Parvalbumin Neuron Stimulation-Evoked Network Activity Despite Recovery of Dendritic Structure and Excitability in the Somatosensory Cortex following Global Ischemia in Mice. *J. Neurosci.* **34**, 14890–14900 (2014).

36. Povysheva, N., Nigam, A., Brisbin, A. K., Johnson, J. W. & Barrionuevo, G. Oxygen–Glucose Deprivation Differentially Affects Neocortical Pyramidal Neurons and Parvalbumin-Positive Interneurons. *Neuroscience* **412**, 72–82 (2019).

37. Balbi, M. *et al.* Gamma frequency activation of inhibitory neurons in the acute phase after stroke attenuates vascular and behavioral dysfunction. *Cell Rep* **34**, 108696 (2021).

38. Kenigsbuch, M. *et al.* A shared disease-associated oligodendrocyte signature among multiple CNS pathologies. *Nat Neurosci* **25**, 876–886 (2022).

39. Leng, K. *et al.* CRISPRi screens in human iPSC-derived astrocytes elucidate regulators of distinct inflammatory reactive states. *Nat Neurosci* **25**, 1528–1542 (2022).

40. Habib, N. *et al.* Disease-associated astrocytes in Alzheimer's disease and aging. *Nat Neurosci* **23**, 701–706 (2020).

41. Li, C. *et al.* Temporal and spatial cellular and molecular pathological alterations with single-cell resolution in the adult spinal cord after injury. *Signal Transduct Target Ther* **7**, 65 (2022).

42. Wei, Y. *et al.* Aerobic glycolysis is the predominant means of glucose metabolism in neuronal somata, which protects against oxidative damage. *Nat Neurosci* **26**, 2081–2089 (2023).

43. Jin, S. *et al.* Inference and analysis of cell-cell communication using CellChat. *Nat Commun* **12**, 1088 (2021).

44. Jin, S., Plikus, M. V. & Nie, Q. CellChat for systematic analysis of cell-cell communication from single-cell and spatially resolved transcriptomics. 2023.11.05.565674 Preprint at https://doi.org/10.1101/2023.11.05.565674 (2023).

45. Huttner, H. B. *et al.* The age and genomic integrity of neurons after cortical stroke in humans. *Nat Neurosci* **17**, 801–803 (2014).

46. He, F. *et al.* Multimodal mapping of neural activity and cerebral blood flow reveals long-lasting neurovascular dissociations after small-scale strokes. *Science Advances* **6**, eaba1933 (2020).

47. Khalil, A. A. *et al.* Non-invasive monitoring of longitudinal changes in cerebral hemodynamics in acute ischemic stroke using BOLD signal delay. *J Cereb Blood Flow Metab* **40**, 23–34 (2020).

48. Kaplan, L., Chow, B. W. & Gu, C. Neuronal regulation of the blood–brain barrier and neurovascular coupling. *Nat Rev Neurosci* **21**, 416–432 (2020).

49. Mascaro, A. L. A. *et al.* Combined Rehabilitation Promotes the Recovery of Structural and Functional Features of Healthy Neuronal Networks after Stroke. *Cell Reports* **28**, 3474-3485.e6 (2019).

50. Ding, J. B., Oh, W.-J., Sabatini, B. L. & Gu, C. Semaphorin 3E–Plexin-D1 signaling controls pathway-specific synapse formation in the striatum. *Nat Neurosci* **15**, 215–223 (2012).

51. Zhou, Y.-F. *et al.* Sema3E/PlexinD1 inhibition is a therapeutic strategy for improving cerebral perfusion and restoring functional loss after stroke in aged rats. *Neurobiol Aging* **70**, 102–116 (2018).

52. Yu, R. *et al.* Vascular Sema3E-Plexin-D1 Signaling Reactivation Promotes Post-stroke Recovery through VEGF Downregulation in Mice. *Transl. Stroke Res.* **13**, 142–159 (2022).

53. Overman, J. J. *et al.* A role for ephrin-A5 in axonal sprouting, recovery, and activity-dependent plasticity after stroke. *Proceedings of the National Academy of Sciences* **109**, E2230–E2239 (2012).

54. Dias, D. O. *et al.* Pericyte-derived fibrotic scarring is conserved across diverse central nervous system lesions. *Nat Commun* **12**, 5501 (2021).

55. Liddelow, S. A. *et al.* Neurotoxic reactive astrocytes are induced by activated microglia. *Nature* **541**, 481–487 (2017).

56. Shi, X. *et al.* Stroke subtype-dependent synapse elimination by reactive gliosis in mice. *Nat Commun* **12**, 6943 (2021).

57. Anderson, M. A. *et al.* Astrocyte scar formation aids central nervous system axon regeneration. *Nature* **532**, 195–200 (2016).

58. Dias, D. O. *et al.* Reducing Pericyte-Derived Scarring Promotes Recovery after Spinal Cord Injury. *Cell* **173**, 153-165.e22 (2018).

59. Li, L., Welser, J. V. & Milner, R. Absence of the αvβ3 integrin dictates the time-course of angiogenesis in the hypoxic central nervous system: accelerated

endothelial proliferation correlates with compensatory increases in α5β1 integrin expression. *J Cereb Blood Flow Metab* **30**, 1031–1043 (2010).

60. Lee, C. Z., Xue, Z., Zhu, Y., Yang, G.-Y. & Young, W. L. Matrix metalloproteinase-9 inhibition attenuates vascular endothelial growth factor-induced intracerebral hemorrhage. *Stroke* **38**, 2563–2568 (2007).

61. Li, L., Liu, F., Welser-Alves, J. V., McCullough, L. D. & Milner, R. Upregulation of Fibronectin and the α5β1 and αvβ3 Integrins on Blood Vessels within the Cerebral Ischemic Penumbra. *Exp Neurol* **233**, 283–291 (2012).

62. Lagos-Cabré, R. *et al.* αVβ3 Integrin regulates astrocyte reactivity. *J Neuroinflammation* **14**, 194 (2017).

63. Johnson, K. M., Milner, R. & Crocker, S. J. Extracellular matrix composition determines astrocyte responses to mechanical and inflammatory stimuli. *Neurosci Lett* **600**, 104–109 (2015).

64. Chu, P.-H. *et al.* Astrocyte-associated fibronectin promotes the proinflammatory phenotype of astrocytes through β1 integrin activation. *Molecular and Cellular Neuroscience* **125**, 103848 (2023).

65. Slack, R. J., Macdonald, S. J. F., Roper, J. A., Jenkins, R. G. & Hatley, R. J. D. Emerging therapeutic opportunities for integrin inhibitors. *Nat Rev Drug Discov* **21**, 60–78 (2022).

66. Xu, L. & Yao, Y. Central Nervous System Fibroblast-Like Cells in Stroke and Other Neurological Disorders. *Stroke* **52**, 2456–2464 (2021).

67. O'Leary, L. A. *et al.* Characterization of Vimentin-Immunoreactive Astrocytes in the Human Brain. *Frontiers in Neuroanatomy* **14**, (2020).

68. Liu, Z. *et al.* Beneficial Effects of GFAP/Vimentin Reactive Astrocytes for Axonal Remodeling and Motor Behavioral Recovery in Mice after Stroke. *Glia* **62**, 2022–2033 (2014).

69. Kelly, K. K. *et al.* Col1a1+ perivascular cells in the brain are a source of retinoic acid following stroke. *BMC Neuroscience* **17**, 49 (2016).

70. Shimamura, M. *et al.* Long-term expression of periostin during the chronic stage of ischemic stroke in mice. *Hypertens Res* **37**, 494–499 (2014).

71. Ma, Q. *et al.* PDGFR-α inhibition preserves blood-brain barrier after intracerebral hemorrhage. *Annals of Neurology* **70**, 920–931 (2011).

72. Göritz, C. *et al.* A Pericyte Origin of Spinal Cord Scar Tissue. *Science* **333**, 238–242 (2011).

73. Pietilä, R. *et al.* Molecular anatomy of adult mouse leptomeninges. *Neuron* **0**, (2023).

74. DeSisto, J. *et al.* Single-Cell Transcriptomic Analyses of the Developing Meninges Reveal Meningeal Fibroblast Diversity and Function. *Dev Cell* **54**, 43-59.e4 (2020).

75. Zhao, K. *et al.* microRNA-181a Promotes Mitochondrial Dysfunction and Inflammatory Reaction in a Rat Model of Intensive Care Unit-Acquired Weakness by Inhibiting IGFBP5 Expression. *J Neuropathol Exp Neurol* **81**, 553–564 (2022).

76. Nguyen, X.-X., Muhammad, L., Nietert, P. J. & Feghali-Bostwick, C. IGFBP-5 Promotes Fibrosis via Increasing Its Own Expression and That of Other Pro-fibrotic Mediators. *Front Endocrinol (Lausanne)* **9**, 601 (2018).

77. Vijayan, A. *et al.* IGFBP-5 enhances epithelial cell adhesion and protects epithelial cells from TGFβ1-induced mesenchymal invasion. *Int J Biochem Cell Biol* **45**, 2774–2785 (2013).

78. Han, N. *et al.* Local application of IGFBP5 protein enhanced periodontal tissue regeneration via increasing the migration, cell proliferation and osteo/dentinogenic differentiation of mesenchymal stem cells in an inflammatory niche. *Stem Cell Res Ther* **8**, 210 (2017).

79. Kim, K. S. *et al.* Induction of cellular senescence by insulin-like growth factor binding protein-5 through a p53-dependent mechanism. *Mol Biol Cell* **18**, 4543–4552 (2007).

80. Nam, T. J., Busby, W. H., Rees, C. & Clemmons, D. R. Thrombospondin and osteopontin bind to insulin-like growth factor (IGF)-binding protein-5 leading to an alteration in IGF-I-stimulated cell growth. *Endocrinology* **141**, 1100–1106 (2000).

81. Matsui, Y. *et al.* Osteopontin deficiency attenuates atherosclerosis in female apolipoprotein E-deficient mice. *Arterioscler Thromb Vasc Biol* **23**, 1029–1034 (2003).

82. Pilewski, J. M., Liu, L., Henry, A. C., Knauer, A. V. & Feghali-Bostwick, C. A. Insulin-Like Growth Factor Binding Proteins 3 and 5 Are Overexpressed in Idiopathic Pulmonary Fibrosis and Contribute to Extracellular Matrix Deposition. *Am J Pathol* **166**, 399–407 (2005).

83. Song, F. *et al.* Deletion of endothelial IGFBP5 protects against ischaemic hindlimb injury by promoting angiogenesis. *Clin Transl Med* **14**, e1725 (2024).

84. Rust, R. Insights into the dual role of angiogenesis following stroke. *J. Cereb. Blood Flow Metab.* **40**, 1167–1171 (2020).

85. Zaremba, J., Skrobański, P. & Losy, J. The level of chemokine CXCL5 in the cerebrospinal fluid is increased during the first 24 hours of ischaemic stroke and correlates with the size of early brain damage. *Folia Morphol (Warsz)* **65**, 1–5 (2006).

86. Stanne, T. M. *et al.* Longitudinal Study Reveals Long-Term Proinflammatory Proteomic Signature After Ischemic Stroke Across Subtypes. *Stroke* **53**, 2847–2858 (2022).

87. Fukuda, S. *et al.* Focal cerebral ischemia induces active proteases that degrade microvascular matrix. *Stroke* **35**, 998–1004 (2004).

88. Hamann, G. F. *et al.* Microvascular basal lamina injury after experimental focal cerebral ischemia and reperfusion in the rat. *J Cereb Blood Flow Metab* **22**, 526–533 (2002).

89. Plaisier, E. *et al.* COL4A1 mutations and hereditary angiopathy, nephropathy, aneurysms, and muscle cramps. *N Engl J Med* **357**, 2687–2695 (2007).

90. Kufner, A. *et al.* Magnetic resonance imaging-based changes in vascular morphology and cerebral perfusion in subacute ischemic stroke. *J Cereb Blood Flow Metab* **41**, 2617–2627 (2021).

91. Nih, L. R., Gojgini, S., Carmichael, S. T. & Segura, T. Dual-function injectable angiogenic biomaterial for the repair of brain tissue following stroke. *Nature Materials* **17**, 642 (2018).

92. Escudero, C. *et al.* Vascular endothelial growth factor and poor prognosis after ischaemic stroke. *European Journal of Neurology* **28**, 1759–1764 (2021).

93. Zheng, X. *et al.* Angiopoietin-like protein 4 and clinical outcomes in ischemic stroke patients. *Ann Clin Transl Neurol* **8**, 687–695 (2021).

94. Rust, R. *et al.* Nogo-A is secreted in extracellular vesicles, occurs in blood and can influence vascular permeability. *J Cereb Blood Flow Metab* 0271678X231216270 (2023) doi:10.1177/0271678X231216270.

95. Weber, R. Z. *et al.* A toolkit for stroke infarct volume estimation in rodents. *Neuroimage* 120518 (2024) doi:10.1016/j.neuroimage.2024.120518.

96. Weber, R. Z., Mulders, G., Perron, P., Tackenberg, C. & Rust, R. Molecular and anatomical roadmap of stroke pathology in immunodeficient mice. *Frontiers in Immunology* **13**, (2022).

97. Zhou, Y. *et al.* Human and mouse single-nucleus transcriptomics reveal TREM2-dependent and TREM2-independent cellular responses in Alzheimer's disease. *Nat Med* **26**, 131–142 (2020).

98. Weber, R. Z. *et al.* Human iPSC-derived cell grafts promote functional recovery by molecular interaction with stroke-injured brain. 2024.04.03.588020 Preprint at https://doi.org/10.1101/2024.04.03.588020 (2024).

99. Rust, R. *et al.* Xeno-free induced pluripotent stem cell-derived neural progenitor cells for in vivo applications. *Journal of Translational Medicine* **20**, 421 (2022).

100. Weber, R. *et al.* Intracerebral Transplantation and In Vivo Bioluminescence Tracking of Human Neural Progenitor Cells in the Mouse Brain | Protocol. *JoVE (Journal of Visualized Experiments)* **(in press)**, (2022).